J. Fluid Mech. (2011), *vol.* 672, *pp.* 521–544.
doi:10.1017/S0022112010006129

Symmetry breaking and instability mechanisms in medium depth torsionally driven open cylinder flows

STUART J. COGAN†, KRIS RYAN AND GREGORY J. SHEARD

Fluids Laboratory for Aeronautical and Industrial Research (FLAIR), Department of Mechanical and Aerospace Engineering, Monash University, Melbourne 3800, Australia

(Received 29 March 2010; revised 12 October 2010; accepted 22 November 2010; first published online 14 February 2011)

A numerical investigation was conducted into the different flow states, and bifurcations leading to changes of state, found in open cylinders of medium to moderate depth driven by a constant rotation of the vessel base. A combination of linear stability analysis, for cylinders of numerous height-to-radius aspect ratios (H/R), and nonlinear stability analysis and three-dimensional simulations for a cylinder of aspect ratio 1.5, has been employed. Attention is focused on the breaking of $SO(2)$ symmetry. A comprehensive map of transition Reynolds numbers as a function of aspect ratio is presented by combining a detailed stability analysis with the limited existing data from the literature. For all aspect ratios considered, the primary instabilities are identified as symmetry-breaking Hopf bifurcations, occurring at Reynolds numbers well below those of the previously reported axisymmetric Hopf transitions. It is revealed that instability modes with azimuthal wavenumbers $m = 1$, 3 and 4 are the most unstable in the range $1.0 < H/R < 4$, and that numerous double Hopf bifurcation points exist. Critical Reynolds numbers generally increase with cylinder aspect ratio, though a decrease in stability occurs between aspect ratios 1.5 and 2.0, where a local minimum in critical Reynolds number occurs. For $H/R = 1.5$, a detailed characterisation of instability modes is given. It is hypothesized that the primary instability leading to transition from steady axisymmetric flow to unsteady three-dimensional flow is related to deformation of shear layers that are present in the flow, in particular at the interfacial region between the vortex breakdown bubble and the primary recirculation.

Key words: instability, vortex breakdown

1. Introduction

Flows in stationary cylindrical cavities driven by rotation of the vessel base, and the process of vortex breakdown that occurs therein, have been investigated by researchers for many years. These flows have applications in mixing and geophysical flows (Gutman 1957; Vyazmina *et al.* 2009), as a platform for investigations into the vortex breakdown phenomenon (Escudier 1984; Brown & Lopez 1990; Lopez

† Email address for correspondence: stuart.cogan@eng.monash.edu.au

1990; Lopez & Perry 1992; Spohn, Mory & Hopfinger 1993, 1998; Brøns, Voigt & Sørensen 2001; Marques & Lopez 2001; Sotiropoulos & Ventikos 2001; Husain, Shtern & Hussain 2003; Thompson & Hourigan 2003; Mununga *et al.* 2004; Iwatsu 2005; Serre & Bontoux 2007; Lo Jacono *et al.* 2008; Brøns, Thompson & Hourigan 2009; Lo Jacono, Nazarinia & Brøns 2009; Tan *et al.* 2009), in flow stability and fundamental physics (Lopez 1995; Blackburn & Lopez 2000; Brøns *et al.* 2001; Gelfgat, Bar-Yoseph & Solan 2001; Hirsa, Lopez & Miraghaie 2002; Lopez & Marques 2004; Lopez *et al.* 2004; Lopez, Cui & Lim 2006) and, recently, for possible implementation as a bioreactor for cell and tissue culture (Dusting, Sheridan & Hourigan 2004, 2006).

The parameter space and boundary conditions describing the flow are well defined. Furthermore, the flow is independent of both time and the azimuthal coordinate over a large part of the parameter space, which is defined by the height-to-radius aspect ratio, H/R, and the Reynolds number, Re. For relatively low Reynolds numbers, the flow has many interesting features. These include the primary swirling flow, the secondary meridional circulation, vortex breakdown leading to recirculation zones attached to either the axis, free surface, or both, and the presence of shear layers of differing strengths. Several of these features bear a physical relevance to the fields of stagnation theory, topological bifurcations and vortex breakdown (see for example Brøns *et al.* 2001). Free surface dynamics also become important for $H/R \leqslant 1.0$ (Lopez & Marques 2004; Lopez *et al.* 2004) or if the Froude number $Fr = \Omega^2 R^2/gH$, where Ω is the base rotational velocity and g is gravitational acceleration, is not small (that is, if $Fr \sim 1$ or higher) (Spohn *et al.* 1993; Lopez 1995; Brøns *et al.* 2001).

The meridional circulation develops at low Re for all H/R and vortex breakdown can set in at Reynolds numbers as low as $Re \simeq 230$ for $H/R = 0.5$, $Re \simeq 730$ for $H/R = 1.5$ and $Re = 1450$ for $H/R = 2.5$ (Iwatsu 2005). This occurs well before transitions affecting the dimensional dependence of the system set in. There are also numerous topological bifurcations (in terms of the structure, location and number of vortex breakdown bubbles) that do not alter the axisymmetry or time dependence of the system but generally occur before the first transition to time dependence or three-dimensionality. These topological changes of state have been extensively studied experimentally, theoretically and numerically for many different configurations of the basic system, including for the case of an enclosed flow with one endwall rotating (Escudier 1984; Spohn *et al.* 1998; Stevens, Lopez & Cantwell 1999; Sotiropoulos & Ventikos 2001; Thompson & Hourigan 2003), an enclosed flow with both endwalls co-rotating and counter-rotating (Gelfgat, Bar-Yoseph & Solan 1996; Brøns, Voigt & Sørensen 1999), and for an open flow case with base rotation (Spohn *et al.* 1993; Lopez 1995; Brøns *et al.* 2001). The topology of these flows (both open and enclosed) is now well documented and, for the enclosed case, the stability limits of the system with regard to both time dependence and axisymmetry breaking have been identified and verified by a number of researchers for the single rotating base case at numerous discrete aspect ratios (Blackburn & Lopez 2000; Lopez, Marques & Sanchez 2001; Marques & Lopez 2001; Blackburn 2002), and by Lopez *et al.* (2002) for the case of an enclosed flow with rotating cylinder walls and differentially rotating endwall. The work of Gelfgat *et al.* (2001) maps the spatio-temporal stability limits for *enclosed* cylinders with a rotating base, across a wide and quasi-continuous range of the (H/R, Re) parameter space and predicts the flow states reached after successive bifurcations, for a given H/R. These predictions have, for the most part, been supported by subsequent three-dimensional (3D) direct numerical simulations (DNS) and/or experimental investigations (for example Blackburn & Lopez 2002;

Marques, Lopez & Shen 2002; Lopez 2006; Lopez *et al.* 2006; Sørensen, Naumov & Mikkelsen 2006).

In general, the open flow configuration (see figure 1*a*) has not been as thoroughly investigated as has the fixed-lid configuration. In particular, the process of flow transitions from the steady and axisymmetric state to time-dependent 3D states is not known over much of the (H/R, Re) parameter space. While a reasonably well-defined curve for these critical Reynolds numbers, Re_c, as a function of H/R exists for the transition from steady to unsteady flow in the $SO(2)$ invariant (axisymmetric) subspace (Brøns *et al.* 2001; Iwatsu 2005), transitions from axisymmetry for the open cylinder are yet to be defined across much of the parameter space.

For all aspect ratios that *have* been investigated to date for the open cylinder flow ($H/R = 0.25$ by Lopez *et al.* 2004; $H/R \simeq 1.0$ by Lopez & Marques 2004; $H/R = 2.0$ by Hirsa *et al.* 2002 and Lopez *et al.* 2004; and $H/R = 4.0$ by Serre & Bontoux 2007), the breaking of symmetry occurs at Reynolds numbers much lower than the corresponding axisymmetric Hopf bifurcation. Thus, it would appear that reliance upon axisymmetric critical Reynolds numbers for predictions of the flow states in these uninvestigated (in terms of breaking of axisymmetry) H/R cylinders would probably lead to incorrect assumptions. As such, we have considered several additional and hitherto neglected aspect ratios (in terms of axisymmetry breaking) in order to define further the dynamics of the system over an expanded parameter range. The aspect ratios focused on are $H/R = 1.5$, our main aspect ratio of interest, the focus of the 3D study and, together with $H/R = 1.70$ and 1.75, representative of the range $1.0 < H/R < 2.0$ (revealed to be a complex region of the parameter space); and $H/R = 2.5$, 3.0 and 3.5, representative of the range $2.0 < H/R < 4.0$. We also perform linear stability analysis on the cylinder of aspect ratio $H/R = 2.0$, previously investigated by Hirsa *et al.* (2002) and Lopez *et al.* (2004), for validation purposes.

In particular, as mentioned earlier, we are interested in the aspect ratio $H/R = 1.5$ configuration for possible implementation as a naturally aspirated bioreactor (see Dusting *et al.* 2006). Thus, while conducting linear stability analysis at the aforementioned aspect ratios to shed light on the breaking of symmetry for the overall parameter space, we focus most of our attention on the $H/R = 1.5$ case and perform 3D spectral element–Fourier (SE-F) simulations solely for this configuration.

We limit our investigation to those cylinders having $H/R \geqslant 1.5$, allowing us to accurately model the free surface as a flat, stress-free boundary, using a commonly implemented symmetry boundary condition. This has been shown to be satisfactory in what some have labelled 'deep' cylinders, those having $H/R > 1.0$ (Lopez *et al.* 2004). Here we do not investigate the validity of the flat stress-free boundary condition, relying upon evidence that, for cylinders with $H/R > 1.0$, the primary $SO(2)$ symmetry-breaking instability modes do not break the reflection symmetry (Lopez & Marques 2004; Lopez *et al.* 2004), and that departures from a perfectly flat surface are minimal (Spohn *et al.* 1993; Lopez *et al.* 2004; Bouffanais & Lo Jacono 2009), and are thus unlikely to significantly affect either the base flow structures or the instability dynamics. The Froude number (Fr) remained below 0.1 for all combinations of H/R and Re considered. The SE-F simulations serve not only as an excellent tool to gain further details about specific flow states and the underlying physics of the system, but also as a validation of the results predicted by the stability analysis.

The stability analysis for all aspect ratios was conducted in the Reynolds number range $1800 \leqslant Re \leqslant 3800$. This was carried out in order to ascertain, over a wider range of cylinder aspect ratios than has previously been considered, whether or not the supercritical axisymmetric Hopf bifurcation is the primary transition from the

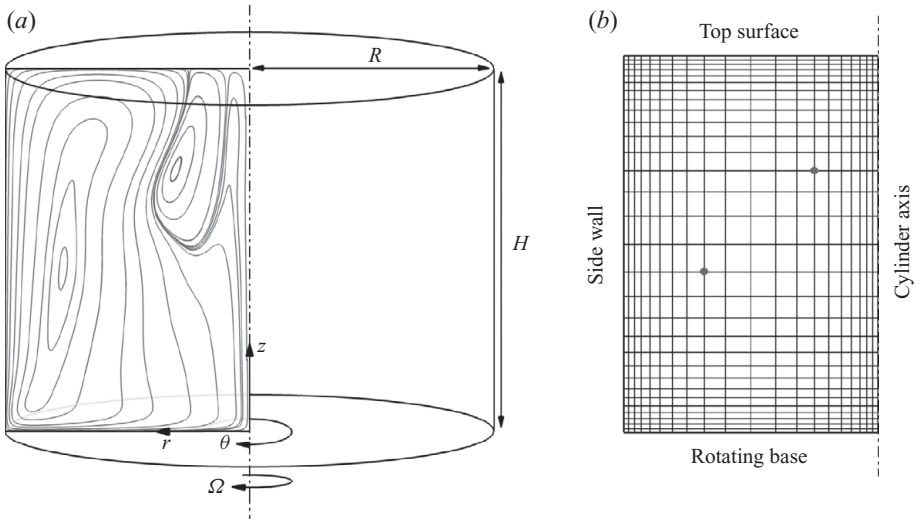

FIGURE 1. (*a*) Schematic diagram of the system under investigation, showing physical parameters and streamlines of the steady axisymmetric base flow at $Re = 2000$ for $H/R = 1.5$; (*b*) grid used for the computations in the meridional semi-plane for the cylinder with $H/R = 1.5$; points monitored for grid independence are indicated. The distribution of elements was similar for all aspect ratios.

basic state, or if the flow undergoes symmetry-breaking bifurcations at lower Re; and if so, what azimuthal wavenumbers are the most critical. Symmetry breaking has been reported at lower Reynolds numbers (relative to any axisymmetric bifurcations) for flows in open cylinders with aspect ratios of 0.25, $\approx$1.0, 2.0 and 4.0 by Lopez *et al.* (2004), Lopez & Marques (2004), Lopez *et al.* (2004) and Serre & Bontoux (2007), respectively. However, Gelfgat *et al.* (2001) have shown that for the *enclosed* cylinder flow, the primary instability can switch back and forth between axisymmetric and non-axisymmetric as H/R is varied in the range $H/R \in [1.0, 4.0]$. In that study, an axisymmetric instability was in fact the primary instability of the basic state for closed cylinders of aspect ratio $1.63 < H/R < 2.76$, and this represents a large part of our own parameter space. This is the first time that this analysis has been reported for open cylinders at the intermediate aspect ratios $1.5 \leqslant H/R \leqslant 3.5$, other than for those with $H/R = 2.0$ (Lopez *et al.* 2004).

The remainder of the article is set out as follows. In § 2, the problem formulation and numerical details are discussed. In § 3, the stability limits and bifurcation map predicted by the linear stability analysis for numerous aspect ratios are presented. Section 4 contains the details of the 3D analysis at $H/R = 1.5$. Conclusions are presented in § 5.

2. Methodology

The system comprises a cylinder of height H and radius R filled with an incompressible Newtonian fluid of kinematic viscosity ν. The system is driven by constant rotation of the bottom endwall of the cylinder at angular velocity Ω. The top of the cylinder is open, leaving the fluid surface exposed. These parameters, and the coordinate system employed, are shown schematically in figure 1, alongside an example of the grids used in conjunction with the spectral-element flow solver. Also shown in figure 1(*a*) are the base flow streamlines for the $H/R = 1.5$ cylinder

	At upper point			At lower point						
p_n	$\lvert u_z\rvert$	$\lvert u_r\rvert$	$\lvert u_\theta\rvert$	$\lvert u_z\rvert$	$\lvert u_r\rvert$	$\lvert u_\theta\rvert$	σ_1	σ_2	σ_3	σ_4
4	0.007688	0.01430	0.01990	0.03406	0.01596	0.03683	1.026	0.8952	0.7627	0.7813
6	0.007671	0.01434	0.01993	0.03411	0.01578	0.03707	1.020	0.8930	0.7620	0.7799
8	0.007672	0.01434	0.01992	0.03412	0.01578	0.03697	1.023	0.8933	0.7621	0.7801
9	0.007672	0.01435	0.01992	0.03412	0.01578	0.03696	1.023	0.8933	0.7621	0.7801
10	0.007672	0.01434	0.01992	0.03412	0.01577	0.03696	1.023	0.8933	0.7621	0.7802

TABLE 1. Convergence in the magnitude of local velocity fluctuations at the points shown in figure 1(*b*), along with the growth rates of the leading linear instability modes for azimuthal wavenumbers $m = 1$, 2, 3 and 4, with polynomial degree p_n. Results shown are for $H/R = 1.5$ at $Re = 3000$.

at $Re = 2000$, just prior to the onset of instability. The characteristic length of the system is the aspect ratio, H/R, which we vary in the range $1.5 \leqslant H/R \leqslant 3.5$. The other parameter required to fully define the system is the Reynolds number, defined as

$$Re = \frac{R^2\Omega}{\nu}, \tag{2.1}$$

which is varied in the range $1800 \leqslant Re \leqslant 3800$.

2.1. *Numerical treatment*

In this study, lengths are normalised by the cylinder radius R, velocities by $R\Omega$ and time by $1/\Omega$. Conservation of momentum and mass for our system yields the unsteady incompressible Navier–Stokes equations, written here in the dimensionless vector form as

$$\frac{\partial \boldsymbol{u}}{\partial t} + (\boldsymbol{u}\cdot\nabla)\boldsymbol{u} = -\nabla P + \frac{1}{Re}\nabla^2\boldsymbol{u}, \tag{2.2}$$

and the continuity equation

$$\nabla\cdot\boldsymbol{u} = 0, \tag{2.3}$$

where $\boldsymbol{u} = (u_z,u_r,u_\theta)(z,r,\theta)$ is the velocity field, z, r and θ are respectively the axial, radial and azimuthal coordinates, t is time and $P = p/\rho$ is the kinematic pressure field, where p is the pressure and ρ is the fluid density.

A spectral-element solver (Sheard & Ryan 2007; Sheard, Fitzgerald & Ryan 2009) is used in all computations: axisymmetric base flows, linear stability analysis and SE-F simulations. For cylindrical geometries, the package utilizes a nodal spectral-element method for spatial discretisation of the flow field in the meridional (r, z) plane. Within each spectral element, the flow variables $(\boldsymbol{u}, P)$ are computed at Gauss–Legendre–Lobatto quadrature points, using polynomial shape functions of degree p_n.

Grid independence was verified through a p-type resolution study. Numerous quantities were monitored including local velocity and pressure at the two points in the domain shown in figure 1(*b*) (for grid independence of base flows), and the leading Floquet multiplier for each azimuthal wavenumber (for grid independence of the linear stability results). Convergence to four significant digits was achieved for polynomial basis functions of degree $p_n \geqslant 8$, as shown in table 1. We employed basis functions of degree $p_n = 9$ together with meshes containing between 600 and 1120 elements, depending on aspect ratio, for all simulations reported herein. A Fourier expansion is implemented to resolve the flow in the azimuthal direction, in a fashion

similar to the formulation given by Blackburn & Sherwin (2004). Up to $N_p = 36$ Fourier planes were used in the azimuthal direction for the highest-Reynolds-number SE-F simulations.

Equations (2.2) and (2.3) are integrated forward in time using an operator-splitting technique based on the third-order accurate backward differentiation (Karniadakis, Israeli & Orszag 1991). These packages have been employed recently by Sheard & Ryan (2007), Sheard (2009) and Sheard *et al.* (2009), and more information on the solver may be found in those articles. The boundary conditions enforced are: no slip at the vertical sidewalls, $(u_z, u_r, u_\theta) = 0$; a steady single component velocity $(u_z, u_r, u_\theta) = (0, 0, r\Omega)$ at the rotating base; and a flat stress-free constraint on the surface, achievable by implementing a symmetry condition $u_z = \partial u_r/\partial z = \partial u_\theta/\partial z = 0$ at the upper boundary of the domain. For the axisymmetric base flow simulations, only one half of the meridional plane is modelled, with a symmetry condition at the axis and all of the azimuthal derivatives in the cylindrical formulation of the Navier–Stokes equations set to zero.

A linear stability analysis based on the Floquet theorem for second-order linear differential equations is applied to the linearised Navier–Stokes equations in order to ascertain the stability of the axisymmetric base flow solutions to perturbations in the azimuthal direction, across a broad range of aspect ratios. The Navier–Stokes equations are linearised by replacing the velocity field $\boldsymbol{u}$ with the sum of a mean velocity field $\boldsymbol{U}$ and a small perturbation velocity $\boldsymbol{u}'$, i.e. $\boldsymbol{u} = \boldsymbol{U} + \boldsymbol{u}'$, and neglecting terms that are quadratic in $\boldsymbol{u}'$, as these are assumed to be exceedingly small. This produces a set of equations for the perturbation field identical to the Navier–Stokes equations except for the perturbation field advection operator which is no longer nonlinear in $\boldsymbol{u}'$ and takes the form $-(\boldsymbol{U}\cdot\nabla)\boldsymbol{u}' - (\boldsymbol{u}'\cdot\nabla)\boldsymbol{U}$. If the base flow is in a converged (steady) state, it can be 'frozen' in time and need not be evolved with the perturbation field; if the base flow is in a saturated (time-periodic) state, it must be evolved in parallel with the perturbation field. The perturbation field is then monitored for growth from a random initial state over a number of base flow periods (arbitrary for steady base flows) until a selected number of the leading Floquet multipliers (eigenvalues of the perturbation field) for a given azimuthal wavenumber have converged. Calculations are performed using eigenvalue solvers based on either the power method (Sheard & Ryan 2007) or an Arnoldi method (Barkley & Henderson 1996; Blackburn & Lopez 2003), capable of accurately resolving the magnitudes of complex multipliers, as well as their real and imaginary components.

3. Linear stability analysis: bifurcations as a function of H/R

Linear stability analysis was performed on the axisymmetric flows inside cylinders with $H/R = 1.5$, 1.7, 1.75, 2.0, 2.5, 3.0 and 3.5 in the Reynolds number range $Re \in [1800, 3800]$. Depending on the Reynolds number, the axisymmetric base flows were either steady or time-periodic; flows at Reynolds numbers above the first Hopf bifurcation in the axisymmetric subspace were in a saturated periodic state, while those below were steady. The axisymmetric Hopf bifurcation for $H/R = 1.5$ was found to occur at $Re = 2659$.

The results of the linear stability analysis for the cylinder with $H/R = 1.5$ are presented in figure 2, for the Reynolds number range $2100 \leqslant Re \leqslant 2800$. From the figure, it can be seen that for $H/R = 1.5$, linear theory predicts that the flow loses stability through a symmetry-breaking transition due to a mode with azimuthal wavenumber $m = 1$. This bifurcation is a Hopf bifurcation and leads to a rotating

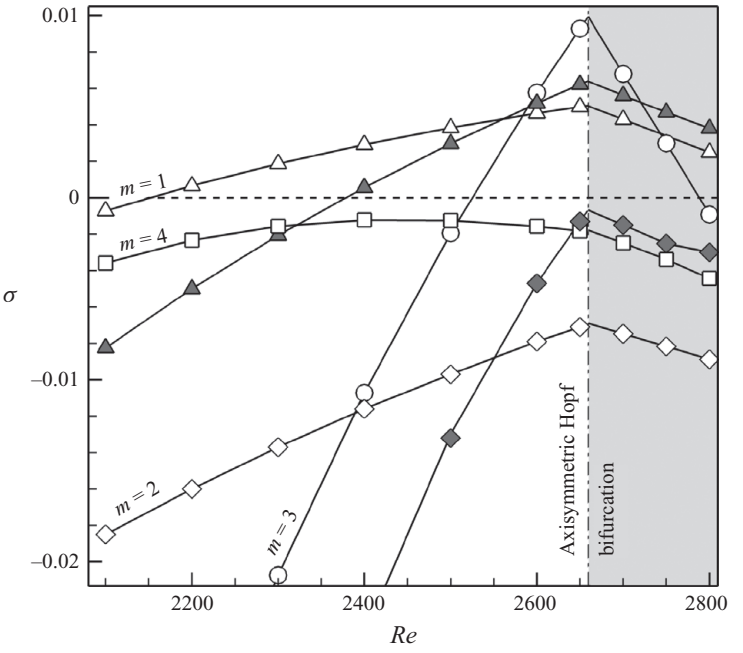

FIGURE 2. Growth rates of the most critical individual modes for the $H/R = 1.5$ cylinder. Different symbol shapes represent different azimuthal wavenumbers. △, $m = 1$; ◇, $m = 2$; ○, $m = 3$; □, $m = 4$. Filled symbols are used to denote a secondary mode at the same wavenumber. The location of the axisymmetric Hopf bifurcation is indicated.

wave state. The transition is predicted to occur at $Re = 2152$, significantly earlier than the axisymmetric transition ($m = 0$) that has been identified previously and found to occur at approximately $Re = 2650$ (Lopez 1995; Brøns *et al.* 2001; Iwatsu 2005), and that was found to occur at $Re = 2659$ during our investigation.

As the Reynolds number is increased, two additional $m = 1$ modes are predicted to become active at $Re = 2379$ and $Re = 2524$, before a mode with azimuthal wavenumber $m = 3$ is predicted to grow at $Re = 2525$ (the tertiary $m = 1$ mode is not included in figure 2 as its growth rate was below the primary and secondary $m = 1$ modes for all Re considered). The secondary $m = 1$ mode gains ascendancy briefly at $Re = 2561$ before the $m = 3$ mode is predicted to become dominant at $Re = 2589$. At the Reynolds numbers immediately above the axisymmetric Hopf bifurcation, the stability analysis predicts decreasing growth rates, leading to eventual decay, of all the modes plotted in figure 2. Other modes (not plotted) had increasing growth rates in this regime, but remained subcritical for all $Re \leqslant 3800$ at $H/R = 1.5$. Linear extrapolation using the two data points from either side of the axisymmetric Hopf bifurcation (for each of the curves in figure 2), to predict the critical Reynolds number for this transition, gives very good agreement with previous findings (Lopez 1995; Brøns *et al.* 2001; Iwatsu 2005).

The growth rates of the leading Floquet modes with $m = 2$ and $m = 4$ that were previously found to lead to symmetry breaking in open cylinders with $H/R = 1.0$ (Lopez & Marques 2004) and $H/R = 2.0$ (Lopez *et al.* 2004), respectively, are also included (for the $H/R = 1.5$ cylinder) in figure 2. For the case of $H/R = 1.5$, these wavenumbers were not observed to support the growth of instability modes within the parameter range considered ($Re \leqslant 3800$).

	Re_c for each H/R						
m	1.5	1.7	1.75	2.0	2.5	3.0	3.5
1	2152	2430	2440	2494	3772	–	–
2	–	2887	2931	3590	2825	2661	2566
3	2525	2410	2292	2070	2072	2167	2355
4	–	2060	2019	1922	2020	2244	2536

TABLE 2. Neutral or critical Reynolds numbers (Re_c) for azimuthal modes $m = 1$, 2, 3 and 4 at each aspect ratio in the Reynolds number range $1800 \leqslant Re \leqslant 3800$.

Growth rates for all modes, at all cylinder aspect ratios, were found to be very small across the entire Reynolds number range considered. In an experimental setting or practical application, these transitions would require a long transient period to manifest. In reality, however, small disturbances from the system exterior will affect even the most carefully isolated and well-crafted system and lead to early onset of these instabilities.

An analysis similar to that outlined above was also performed for cylinders with aspect ratios $H/R = 1.7$, 1.75, 2.0, 2.5, 3.0 and 3.5. The results are summarised in table 2 and presented graphically in the form of a bifurcation map in figure 3. In the figure, the results of the present analysis are represented by filled symbols, while a selection of results from previous studies is shown by hollow symbols in order to provide a more complete map.

The present stability analysis confirms that both the critical Reynolds number Re_c and the first-occurring instability mode wavenumber m_c are strongly dependent on the parameter H/R. Significantly, in contrast to the fixed-lid case, these modes are axisymmetry-breaking across the whole parameter space $0.25 \leqslant H/R \leqslant 4.0$. It can be seen that the predicted symmetry-breaking instability can have wavenumber $m = 1$, 2, 3 or 4 depending on the aspect ratio of the system; the critical Re for $m = 0$ lags significantly behind the first one, two or three $m \neq 0$ critical Reynolds numbers throughout the entire range of H/R. Higher wavenumber modes ($m > 4$) are increasingly stable for the range of aspect ratios considered. The critical wavenumber is very sensitive to aspect ratio, especially in the lower range of H/R with wavenumbers 1–4 all appearing as the most unstable mode before the aspect ratio has reached $H/R = 2.0$, the order of appearance being $m = 3$, 2, 1, 4. The critical wavenumber appears to stabilise somewhat at $m = 4$ from $H/R \simeq 1.6$ to $H/R \simeq 2.75$, and then at $m = 3$ over the remainder of the range of H/R presented in figure 3. Modes with $m = 3$ appear particularly prevalent, being either the first or second most unstable mode over much of the parameter space.

In contrast to enclosed cylinders of similar aspect ratios (Gelfgat *et al.* 2001), there is a definite and fairly consistent trend of decreasing stability of the basic state with decreasing aspect ratio. Only the small region $1.6 \lesssim H/R \lesssim 2$ defies this trend, with a local maximum in the critical Reynolds number (i.e. a local region of increased stability) appearing at approximately $H/R = 1.6$. The axisymmetric time-independent flow remains dominant until higher Reynolds numbers in this region of the H/R parameter space than in regions immediately surrounding it. Overall, critical Reynolds numbers were lower for the open cylinder than for the enclosed cylinders at corresponding aspect ratios, indicating that the presence of the free surface inherently detracts from the stability of the system as a whole. This is true up until approximately

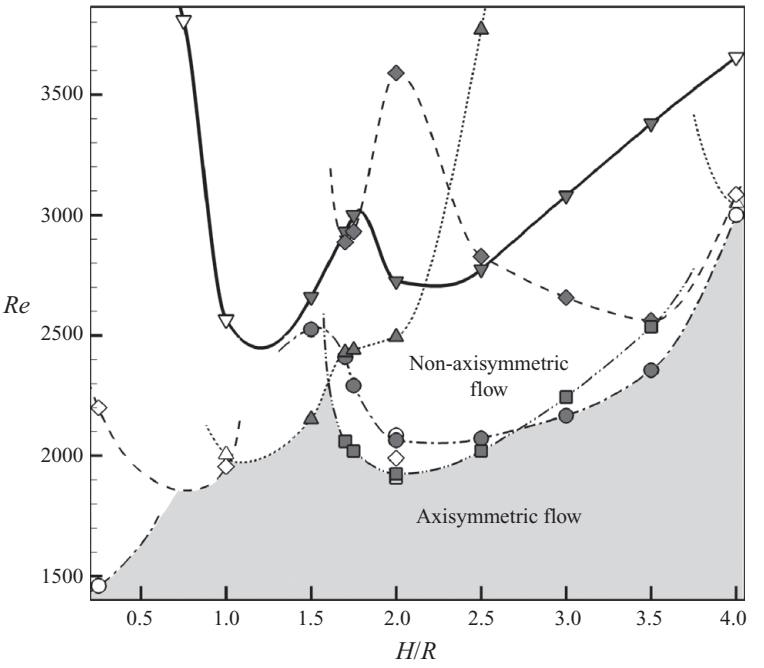

FIGURE 3. Bifurcation map in the H/R–Re parameter space. Symbol shapes represent the same wavenumbers as in figure 2. Solid symbols represent our data points, hollow symbols are used to show the previously published results of others. Hollow ∇ symbols show the location of the axisymmetric Hopf bifurcation for $H/R = 0.75$ and 1.0 (Gelfgat *et al.* 1996; Brøns *et al.* 2001, data averaged), and $H/R = 4.0$ (Brøns *et al.* 2001; Iwatsu 2005, data averaged). Other hollow symbols: $H/R = 0.25$ and 2.0 from Lopez *et al.* (2004), $H/R = 1.0$ from Lopez & Marques (2004) and $H/R = 4.0$ from Serre & Bontoux (2007). The approximate boundary between axisymmetric and non-axisymmetric flow is also shown and guidance lines have been included where appropriate to show possible trends. Different line styles are used to differentiate between trend lines.

$H/R = 3.3$, at which point there is a dramatic drop in the critical Reynolds number for the enclosed cylinder (Gelfgat *et al.* 2001), while for the open cylinder, critical Reynolds numbers continue to increase with increasing aspect ratio up to at least $H/R = 4.0$.

A feature of the bifurcation map for open cylinder flows that is similar to that of the closed cylinder is the existence of a number of multi-bifurcation points, points in the H/R–Re parameter space where it appears that two or more modes of different wavenumber bifurcate from the basic state simultaneously. A number of these points occur at values of H/R, which are strikingly similar between the open and closed cases. These are at $H/R \simeq 1.6$ and $Re \simeq 2300$ in the open cylinder flow (a double bifurcation point exists at $H/R = 1.63$ and $Re \simeq 2700$ in the enclosed cylinder), and at $H/R \simeq 2.75$ and $Re \simeq 2110$, where the open cylinder flow has a double bifurcation point ($H/R = 2.76$ and $Re \simeq 2850$ in the enclosed cylinder). However, in the cases mentioned for the *enclosed* cylinder, the double bifurcation points both involve the axisymmetric $m = 0$ mode, along with the $m = 2$ or $m = 4$ mode respectively, whereas in the *open* cylinder case, they both involve the $m = 4$ mode, along with the $m = 1$ or the $m = 3$ mode, respectively. For the open cylinder, other double bifurcation points exist at approximately [1.02, 1985] involving $m = 1$ and $m = 2$ (located at approximately [1.025, 1950] by Lopez & Marques 2004), and approximately [4.0, 3050] involving

$m=1$ and $m=3$. There is also a double bifurcation point located in the range $0.5 \leqslant H/R < 1.0$ and $1500 < Re < 1500$, involving two out of $m=1$, 2 and 3 (probably 2 and 3), although it is not possible to define this point further with the available data. Lopez & Marques (2004) investigated the competition between modes in the region of the double bifurcation point at [1.025, 1950], shown at [1.02, 1985] in figure 3. They showed how wonderfully complex the flow dynamics can be at these points; thus, these interactions are not investigated here nor are the exact locations of these points pursued further; this however could be the subject of future study.

Figure 3 also reveals that the stability analysis for the case of $H/R=2.0$ accurately predicted the primary transition $Re_c=1922$ (cf. the value of 1910 reported by Lopez *et al.* 2004) as well as the mode ($m=4$) leading to transition. However, subsequent bifurcations can be incorrectly predicted due to the linear nature of the method employed. In this case, the stability analysis on the $H/R=2.0$ cylinder flow predicted a secondary bifurcation due to a mode with $m=3$ at approximately $Re=2065$ (filled circle), and that modes with $m=2$ remain inactive until approximately $Re=3590$ (filled diamond); whereas the 3D DNS of Lopez *et al.* (2004) revealed that the bifurcated $m=4$ flow state actually becomes unstable to an $m=2$ mode at approximately $Re=1990$ (hollow diamond at $H/R=2$ in figure 3). Therefore, although we may rely confidently upon stability analysis predictions for primary instabilities, we must regard predictions of subsequent bifurcations with caution and, where possible, perform 3D nonlinear DNS when seeking to fully characterise flows in these regions of the parameter space.

4. Non-axisymmetric flow and instability mechanisms at $H/R=1.5$

Spectral element–Fourier direct numerical simulations were carried out at a number of Reynolds numbers in the range $2000 \leqslant Re \leqslant 2800$, for the cylinder with aspect ratio 1.5, in order to confirm the findings of the linear stability analysis and to gain information about the evolution of, and saturation to, 3D flow states. These simulations also serve as a means of investigating the nature of the physical mechanisms leading to transition, and the effects of nonlinear interactions between instability modes, on the bifurcated flow states. The growth of instability modes and subsequent saturation of non-axisymmetric states was monitored via recording of time histories of a number of physical quantities. We monitored the velocity and pressure (u_z, u_r, u_θ, P) at a number of discrete mesh points, as well as the energies associated with each of the non-axisymmetric Fourier modes. The modal energies were defined here as

$$E_m = \rho \int_{\theta=0}^{\theta=2\pi} \int_{r=0}^{r=1} \int_{z=0}^{z=H} \left(u_{z_m}^2 + u_{r_m}^2 + u_{\theta_m}^2\right) r \, \mathrm{d}z \, \mathrm{d}r \, \mathrm{d}\theta, \tag{4.1}$$

where u_{zm}, u_{rm} and $u_{\theta m}$ represent the mth Fourier mode contribution to the axial, radial and azimuthal components of velocity, respectively.

The growth to saturated 3D flow states from the converged (steady) axisymmetric states, at $Re=2200$ and $Re=2650$, are shown in figures 4(a) and 5(a), respectively. Here, a time history of the axial component of velocity (u_z) at a point in the vortex breakdown bubble region is plotted. With reference to figure 3, the linear stability analysis predicts the dominant disturbances to have azimuthal wavenumbers $m=1$ for $Re=2200$, and $m=3$ for $Re=2650$. Figure 4(b), which shows the modal energies (E_m) associated with each wavenumber m of the first four Fourier modes during the evolution, confirms that the $m=1$ mode is dominant. As predicted by the linear

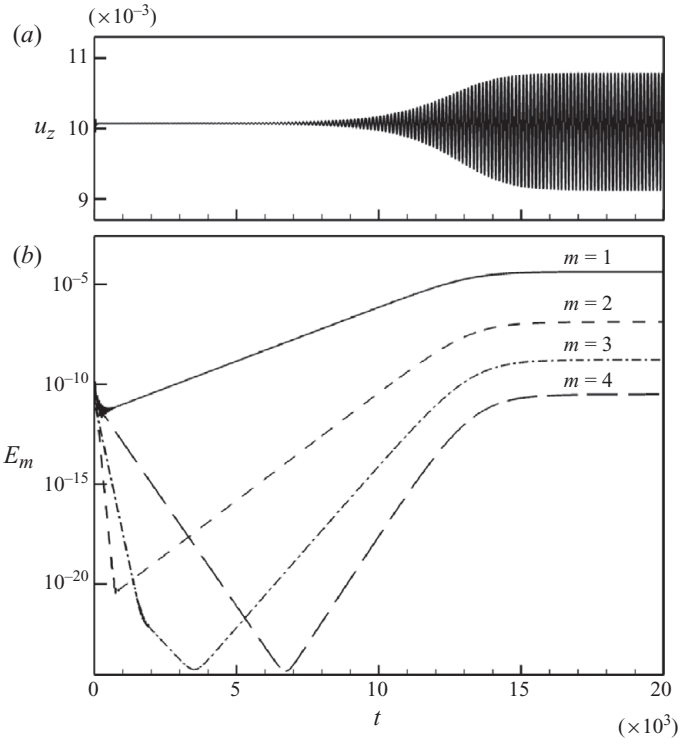

FIGURE 4. (*a*) Time history of the axial component of velocity at a point in the flow for $H/R = 1.5$ showing the growth of the $m = 1$ instability on the axisymmetric base flow at $Re = 2200$. (*b*) Time history of the energy E_m associated with each of the first four Fourier modes m for $Re = 2200$ showing a clearly $m = 1$ dominant flow.

stability analysis, this is the only instability mode whose activity is perceptible at this Reynolds number, with E_2 at least a factor of 100 lower than E_1. However, for the $Re = 2650$ case, the time history indicates a slightly more complicated scenario, with multiple frequencies (produced by multiple instability modes) present in the signal over approximately the first 3500 time units, before the flow saturates to a single periodic state. Figure 5(*b*) shows that a mode with $m = 3$ (predicted by the stability analysis to be dominant at this Re) initially grows with the fastest growth rate, and briefly dominates. A predominantly $m = 3$ flow state is briefly established, which is then unstable to an $m = 1$ mode. This $m = 1$ mode is probably the second $m = 1$ mode shown in figure 2.

Lopez *et al.* (2004) found a similar transient mode with $m = 3$ at $Re = 2200$ during their experiments investigating the transitions of the flow in an open cylinder with $H/R = 2.0$ and at $Re = 2100$ during their numerical analysis of that configuration. The structure of the $m = 3$ mode observed by Lopez *et al.* (2004) is similar but not the same as that of the mode observed in this study (shown in figures 8*a, b* and 9*a*), which is described later. Also, the previously reported $m = 3$ mode was found to break the reflectional (Z_2) symmetry of the system considered by Lopez *et al.* (2004). They considered (numerically) a cylinder of twice the length (compared to the experimental apparatus with $H/R = 2$) both with and without Z_2 symmetry, whereas our system preserves the Z_2 symmetry. Hence, the same $m = 3$ mode identified by Lopez *et al.*

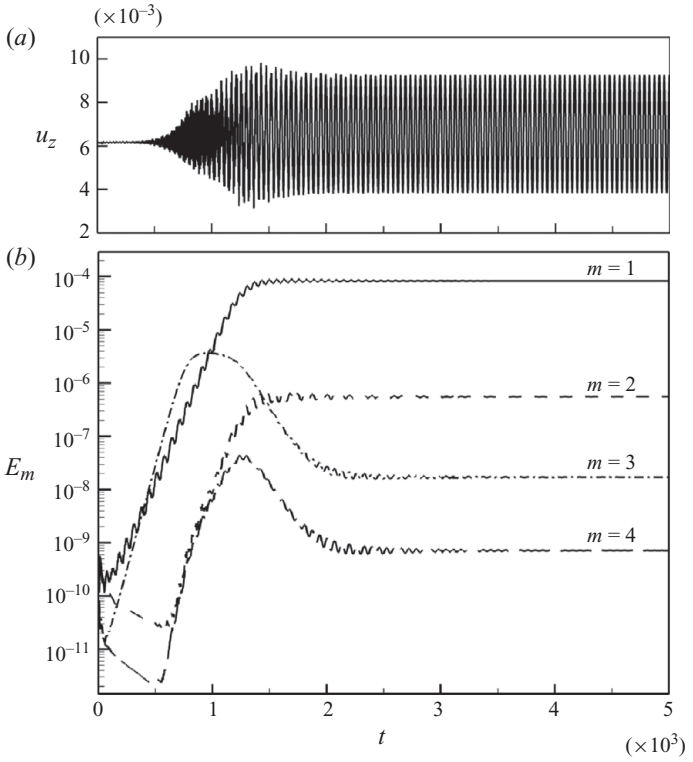

FIGURE 5. (*a*) Time history of the axial component of velocity at a point in the flow for $H/R = 1.5$ showing initial growth of a mixed-mode solution on the axisymmetric base flow before saturation to a single frequency state, for $Re = 2650$. (*b*) Time history of the energy E_m associated with each of the first four Fourier modes m for $Re = 2650$ showing initial growth of the $m = 3$ instability mode before the flow settles to an $m = 1$ dominant state.

(2004) cannot exist in a system such as ours, where Z_2 symmetry is preserved, and the current $m = 3$ mode is a new instability, not previously observed at other aspect ratios.

The results of simulations at $Re = 2200$ and 2650 confirm the initial existence of dominant $m = 1$ and $m = 3$ modes, respectively. Figure 6 shows the growth of the $m = 1$ mode on the axial velocity for an initially axisymmetric flow at $Re = 2200$. The isocontours highlight the major effect of the instability which is to set up a travelling wave on two azimuthally unstable shear layers that exist in the flow: the vortex breakdown bubble shear layer at the interface between the vortex breakdown bubble and the outside flow (dark/negative contours), and the side-wall shear layer (light/positive contours). This figure also alludes to the exceedingly small growth rates predicted by the linear stability analysis. As evidenced in figure 4(*a*), the flow appears steady (and axisymmetric) for a long time both before and after figure 6(*a*) at $t = 1800$; the first signs of asymmetry are observed as a tilting of the shear layer at the vortex breakdown bubble boundary, and a smaller deformation of the (stronger) wall shear layer, for $t \gtrsim 6800$ in this simulation (figure 6*b*). In terms of real time, this would correspond to approximately 1080 base revolutions in a physical experiment

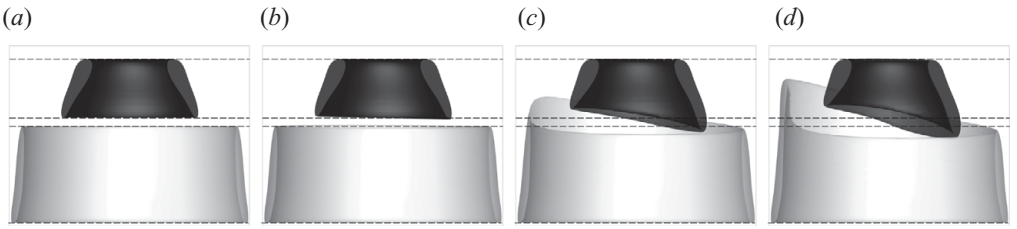

FIGURE 6. Isocontours of the axial velocity, at approximately $\pm 45\,\%$ of the maximum value for $H/R = 1.5$ and $Re = 2200$, at four instances in time showing the evolution of the asymmetry on the axisymmetric base flow in the two regions corresponding to the boundary of the vortex breakdown bubble and the sidewall jet structure. Plots (a), (b), (c) and (d) coincide approximately with times $t = 1800$, 6800, 11 600 and 14 400, in figure 4, respectively.

using, for example, the apparatus described in Lopez *et al.* (2004). From there the growth is exponential with significant increases in the effect of the asymmetry over approximately the following 5000 time units (figure 6c), and then the next 3000 time units (figure 6d), before saturation occurs at $t \simeq 16\,000$. By this time, both shear layers are significantly deformed. The perturbation field axial vorticity (isolated by subtracting the fundamental mode vorticity from the full 3D flow) for the saturated $m = 1$ state from the 3D DNS, at $Re = 2300$, is plotted in figure 7(b) alongside the perturbation field predicted by the linear stability analysis. Excellent agreement in mode structure was obtained, verifying the results of the linear stability analysis for the primary bifurcation and subsequent flow state at $H/R = 1.5$. Some nonlinear effects are evident in the 3D DNS results, most noticeable at intermediate radii ($0.35 < r < 0.75$), and towards the free surface, manifesting as slight deformations of the contour levels predicted by the stability analysis. Most of the instability activity for this $m = 1$ mode appears to be concentrated about the axis of the cylinder, associated with the swirling vortex core in lower regions and the vortex breakdown bubble in the upper regions. Towards $z \simeq 1.0$, significant instability structures at larger radii may be associated with the sidewall shear layer, although it is difficult to ascertain the origin of instability.

Contours of the perturbation axial vorticity for the 3D DNS at $Re = 2650$ are shown in figures 8(b) ($t \simeq 800$) and 8(c) ($t \simeq 4000$), with the mode predicted by stability analysis shown in figure 8(a). These slices correspond to the same axial locations as those highlighted in figure 7. These plots show good agreement between the structure of the $m = 3$ mode predicted by stability analysis and that of the transient $m = 3$ mode observed during DNS. They also confirm the initial dominance of the $m = 3$ mode and subsequently the $m = 1$ mode, and highlight a number of features of the flow at this Reynolds number. At the cylinder base (bottom row, $z = 0.1$) the transient $m = 3$ instability appears quite active at all radii, while the saturated $m = 1$ mode again appears concentrated near the axis; however, the fundamental mode is almost completely dominant in the saturated flow.

In the lower mid-section of the cylinder (second row, $z = 0.5$), the maxima and minima of the $m = 3$ mode are reasonably localised at radii $0.25 \leqslant r \leqslant 0.6$ and this coincides with the radial locations of maximum contour deformations of the resultant flow at this axial height (not shown). At this axial location, the base flow (prior to transition) has streamlines in the meridional plane that, having 'separated' from the vortex breakdown bubble wake, converge with those that did not separate but flowed around the bubble, up the inner tube of the bubble torus and back down the cylinder

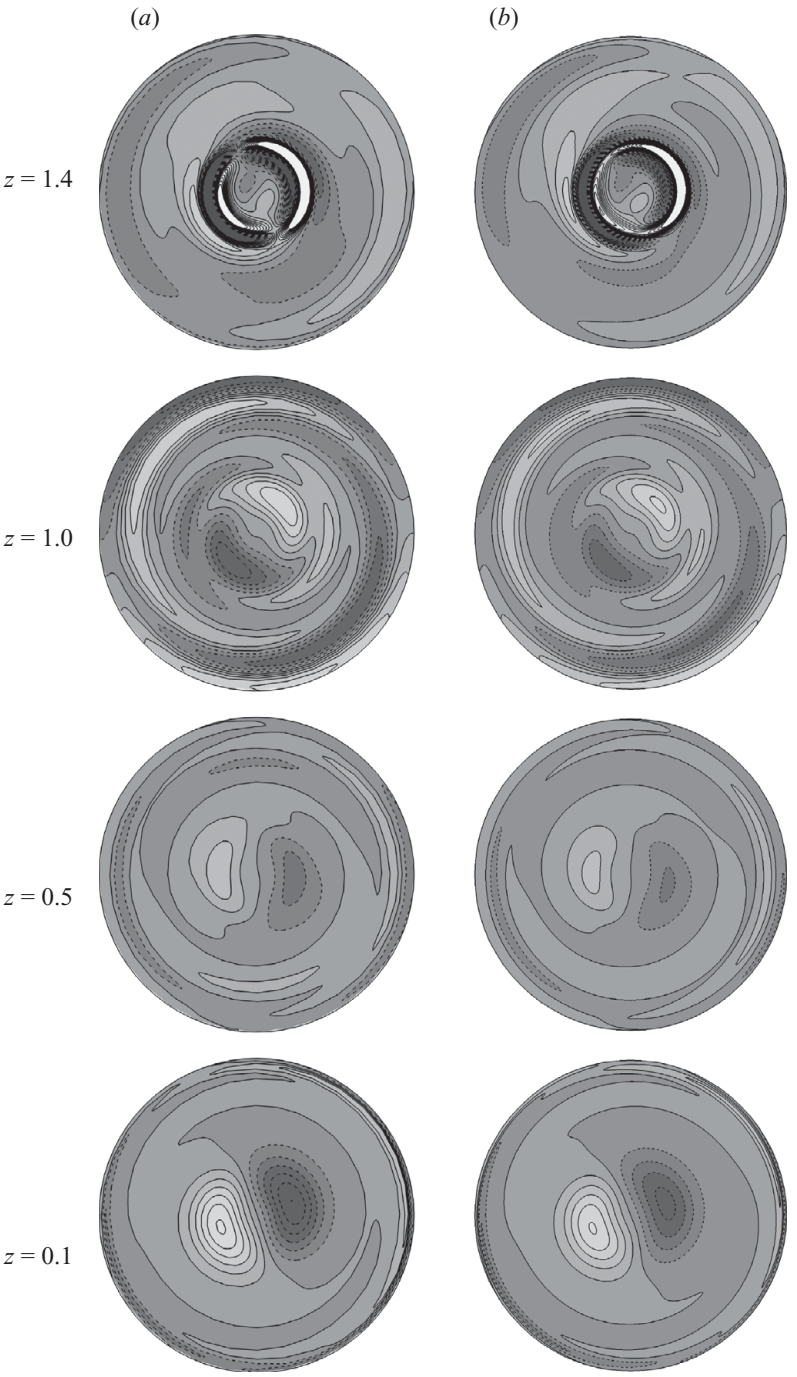

FIGURE 7. Contours of the perturbation axial vorticity for $H/R = 1.5$ generated from the linear-stability analysis predictions at $Re = 2250$ (a) and the 3D simulations at $Re = 2300$ (b), at different axial stations. Rows show different axial locations: $z = 0.1, 0.5, 1.0$ and 1.4, from bottom to top, respectively. Dark grey contours (dashed lines) are negative and light grey contours (solid lines) are positive. The levels are arbitrary for comparison of the perturbation vorticity field structure.

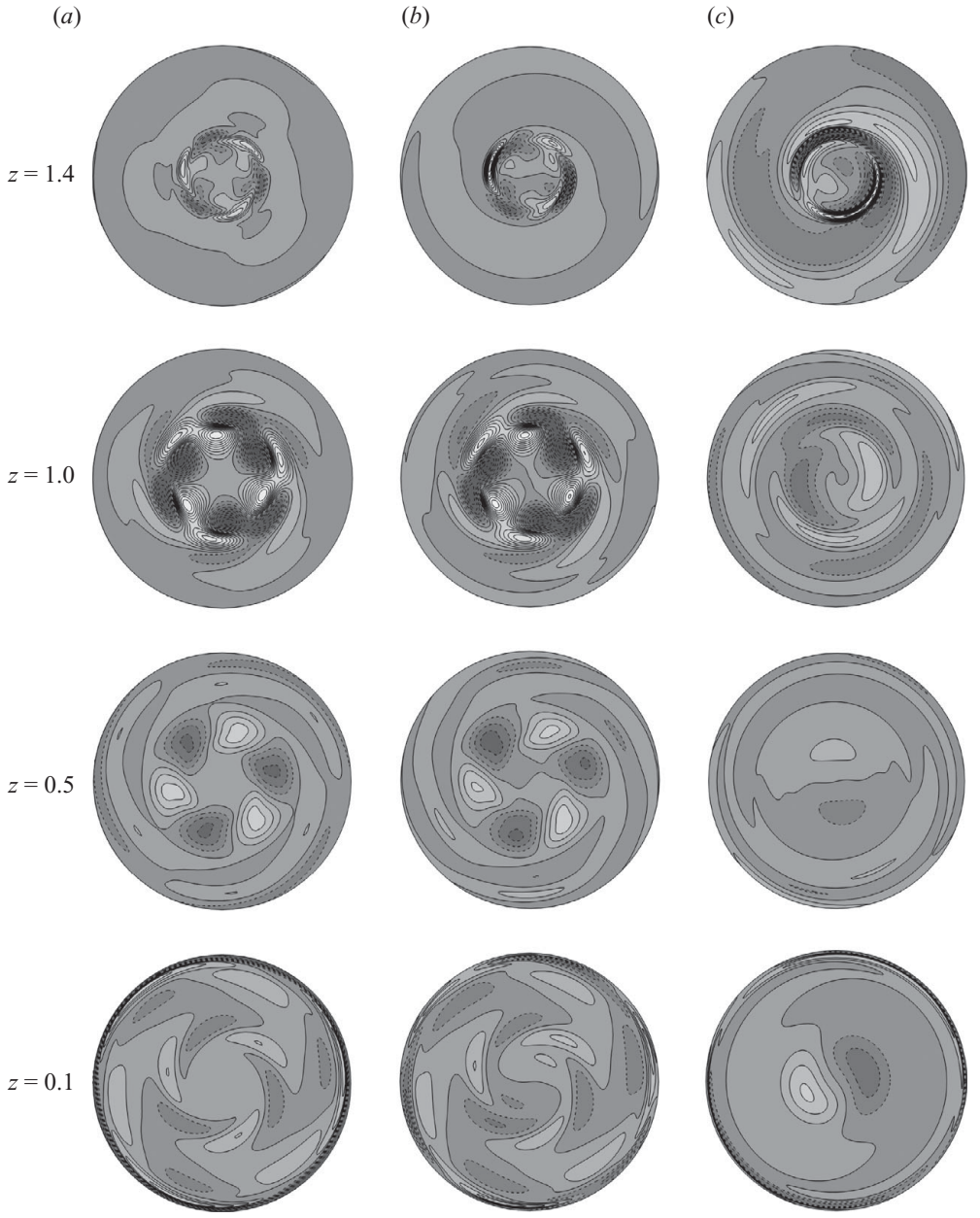

FIGURE 8. Slices through the r–θ plane for, $H/R = 1.5$, showing contours of the perturbation axial vorticity at various axial locations for $Re = 2650$. (*a*) The $m = 3$ mode predicted by the linear stability analysis; (*b*) the transient mixed $m = 3/m = 1$ mode state with dominant $m = 3$ component from DNS at $t \approx 800$; (*c*) the final saturated $m = 1$ mode state from DNS at $t \approx 4800$. Rows show different axial locations: $z = 0.1, 0.5, 1.0$ and 1.4, from bottom to top, respectively. Dark grey contours (dashed lines) are negative and light grey contours (solid lines) are positive. The levels are arbitrary for comparison of the perturbation vorticity field structure.

axis (see streamlines in figure 11*a* for example). At this height, there is a slight $m = 1$ component to the $m = 3$ dominant flow evident at large radii in the outer regions of the cylinder (figure 8*b*).

In the upper mid-section of the cylinder (third row, $z = 1.0$), numerous very intense maxima and minima are present for the $m = 3$ mode in the region $0.2 \leqslant r \leqslant 0.6$, while the saturated $m = 1$ mode (figure 8*c*) is also quite active in the same region. Again, in terms of features of the base flow, this slice corresponds to the axial location of maximum radial width of the vortex breakdown bubble and hence maximum bending of streamlines returning to the cylinder base, in the meridional plane.

Towards the free surface (top row, $z = 1.4$), there is a very distinct localisation of perturbation vorticity maxima and minima in the region $0.13 \leqslant r \leqslant 0.37$. The most significant features of the base flow in this region are the stagnation points where the vortex breakdown bubble meets the free surface, coinciding again with significant bending of streamlines in the meridional plane. At this height, approaching the free surface, the $m = 1$ mode's contribution during the transient phase (figure 8*b*) appears to be of a strength similar to the $m = 3$ component. The final saturated state at $Re = 2650$ ($m = 1$, figure 8*c*) is similar to, but not the same as, the $m = 1$ state at $Re = 2300$ shown in figure 7(*b*). This is most noticeable both at the level of azimuthal displacement of the mode structures between the slices in figure 7(*b*) as compared with those in figure 8(*c*), and in the increase in coherent structures at intermediate radii and decrease of structures at large radii for the higher-Re case compared with the lower Re. This agrees with the predictions of the stability analysis, where figure 2 shows a secondary $m = 1$ mode existing at $Re = 2650$ and only a single $m = 1$ mode at $Re = 2300$. Throughout the cylinder at $Re = 2650$, the majority of asymmetric activity associated with the transiently unstable $m = 3$ and the ultimately unstable $m = 1$ mode is concentrated around the axis and the vortex breakdown bubble, except for at the base where the fundamental ($m = 0$) mode is more dominant. Figure 9 shows isocontours of each component of the perturbation velocity field (u'_r, u'_θ, u'_z) at $Re = 2650$ for the transient $m = 3$ mode (figure 9*a*) and the final saturated $m = 1$ perturbation field (figure 9*b*). Also shown on these plots are slices of the respective velocity components at the same axial locations as in figures 7 and 8. These were obtained by subtracting the zeroth Fourier mode from the full 3D solution at the two instants in time. These plots reveal a complex spatial structure in all cases. As expected, the axial component, u_z, vanishes at the free surface for both modes (a consequence of the non-deforming boundary condition), while the radial and azimuthal components are free to take on finite values at that location. In fact, for the $m = 1$ mode, both radial and azimuthal perturbation velocity components have near-maximum values emanating from the free surface, at the location where the flow returning from the perimeter of the vessel separates from the free surface to flow around the vortex breakdown bubble, and following a line (or surface) along the outer edge of the vortex breakdown bubble a short distance into the interior of the cylinder. In all cases, there is significant activity in the vicinity of the vortex breakdown bubble.

The $m = 1$ mode (figure 9*b*) has noticeable rose-petal-shaped structures attached to the vortex breakdown bubble boundary for all velocity components (identified as structure number one in figure 10). These structures are where the perturbation to the axial and azimuthal velocity fields is maximum (not explicitly shown). The radial component also has this feature, and another region of equal maximum intensity, located near where the rotating vortex core impinges on the rotating base (see figure 9, top–right plot). Attempts to link this region of high perturbation intensity to traditional rotating disk boundary layer instabilities proved unsuccessful and it appears that there is no connection; indeed others have shown (Gregory, Stuart & Walker 1955; Tatro & Mollo-Christensen 1967) that for the Reynolds numbers

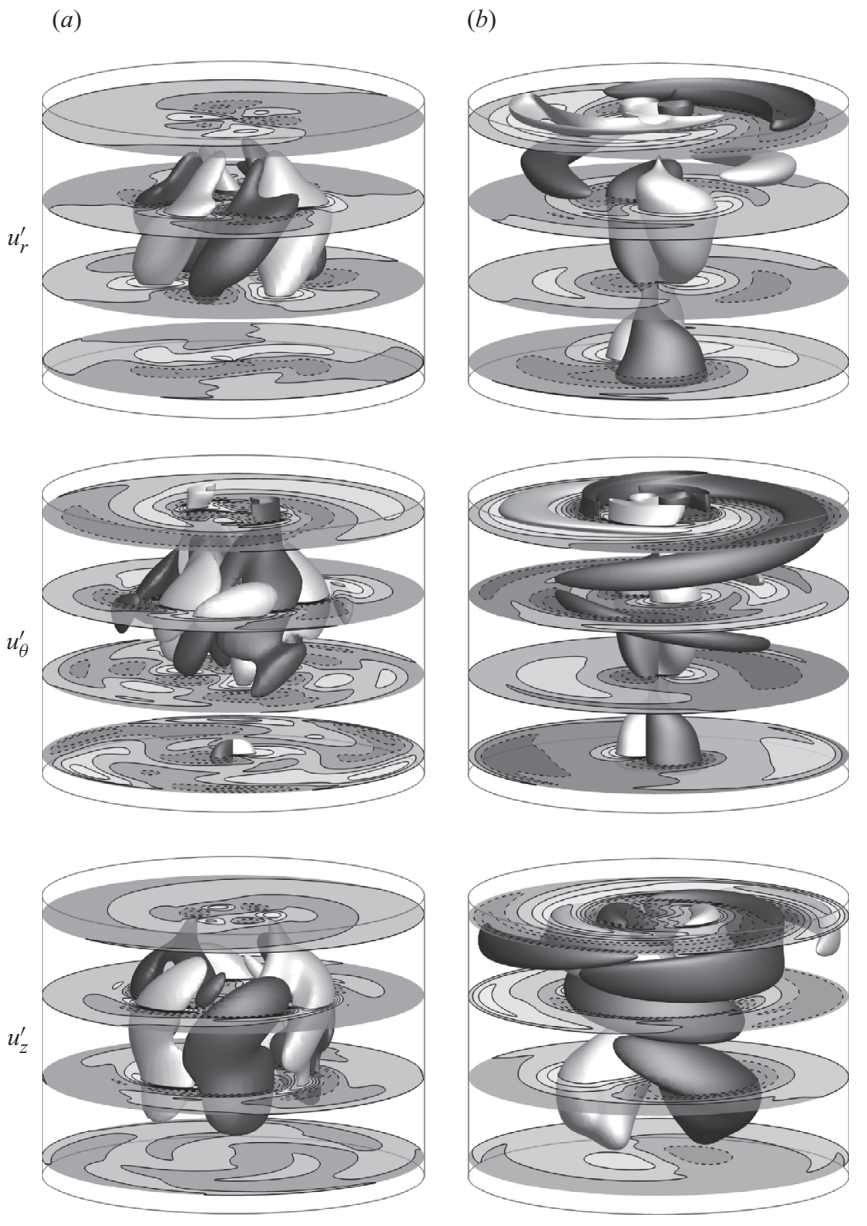

FIGURE 9. Isocontours and slices showing the three components of the perturbation velocity field, for $H/R = 1.5$ at $Re = 2650$. The transient $m = 3$ (*a*) and the saturated $m = 1$ (*b*) modes are shown. Isocontours are at approximately $+33\,\%$ (light grey) and $-33\,\%$ (dark grey) of maximum. Slices have dark grey contours (dashed lines) negative and light grey contours (solid lines) positive, with levels spaced linearly between $\pm 30\,\%$ of maximum. Top, u_r; middle, u_θ; bottom, u_z (axial). Slices are at the same heights as in figures 7 and 8.

considered in this article, the rotating disk boundary layer is stable. Thus, another mechanism is responsible for this instability.

The axial and azimuthal components of velocity also have notable structures, associated with the $m = 1$ perturbation field, in the outer parts of the cylinder, at approximately $3H/5 \leqslant z \leqslant 4H/5$, and it is around this depth that most of the

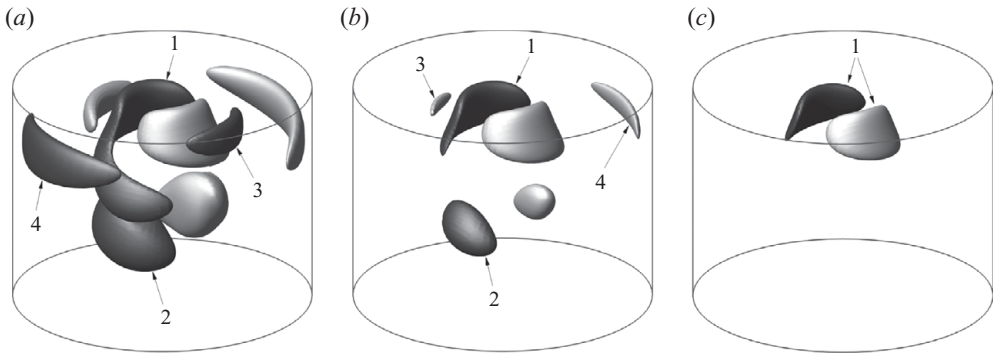

FIGURE 10. Isocontours of the perturbation axial velocity for $H/R = 1.5$ at $Re = 2300$ showing the structure of the saturated state of the $m = 1$ mode at (*a*) 30 %, (*b*) 40 % and (*c*) 50 % of maxima. Dark (light) contours represent negative (positive) values.

instability activity is shown in the slices (for all $m = 1$ velocity components). This region of the cylinder corresponds approximately with the location of maximum radial width of the vortex breakdown bubble and the tip of the associated weak shear layer, as well as with the tip of an intense wall-jet shear layer observed in the outer part of the cylinder. All velocity perturbation components of the $m = 3$ instability appear to cling to the outer edge of the vortex breakdown bubble and shed off into its wake.

These observations would appear to indicate that the physical mechanism leading to the loss of axisymmetry, for both the initial and secondary $m = 1$ and the transient $m = 3$ modes, at this aspect ratio, $H/R = 1.5$, could be instability of the wall-jet shear layer, as suggested by Lopez *et al.* (2004) for the open cylinder with $H/R = 2.0$; but is more likely (for cylinders with $H/R = 1.5$) associated with the vortex breakdown bubble and instability of the shear layer at the interface between the bubble and the primary recirculation. It is also possible that both the wall-jet shear layer, and that associated with the vortex breakdown region, become unstable here at approximately the same Re with the primary $m = 1$ mode growing on the vortex breakdown and the secondary $m = 1$ growing on the wall-jet shear layer. Lopez *et al.* (2004) noted that a secondary instability in the system with $H/R = 2.0$ was closely associated with the recirculation zone, and it may well be that reducing the aspect ratio increases the stability of the wall jet whilst possibly simultaneously de-stabilising the vortex breakdown shear layer.

With respect to the $m = 1$ mode of the current work, the $m = 3$ mode appears to have a far more orderly structure, consisting of overlapping regions of instability precessing about the cylinder axis. There is very little activity in outer regions of the cylinder. All three perturbation velocity components are most energetic within a small localised region (not shown explicitly) that, once again, corresponds with the region of vortex breakdown, and to the tip region of the moderate strength shear layer that exists there. Quantitatively, this region is located in the vicinity of the three points with $r/R = 0.42$ and $z/R = 0.93$, equidistantly spaced in the azimuthal direction (i.e. separated by an angle of $2\pi/3$ rad) and precessing about the cylinder axis.

Figure 10 reinforces the argument that the initial transition is due to an instability involving the interface between the vortex breakdown bubble and the outside flow, and that the weak shear layer at this location drives the growth of the primary instability for cylinders with aspect ratio $H/R = 1.5$. The structures, as numbered in

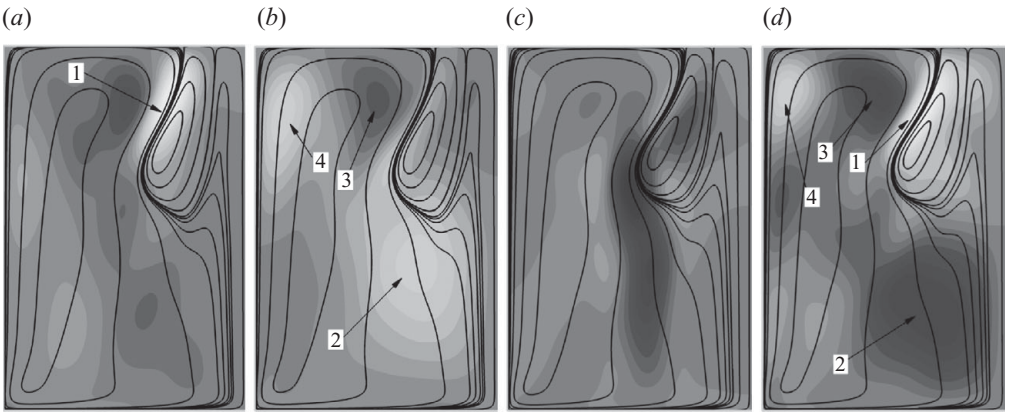

FIGURE 11. Contours of the perturbation axial velocity for $H/R = 1.5$ on one half of the meridional plane, cutting through the (azimuthal) locations of instantaneous maximum instability activity for (*a*) $Re = 2300$, primary structure; (*b*) $Re = 2300$, secondary structures; (*c*) $Re = 2650$, transient $m = 3$ mode; and (*d*) $Re = 2650$, saturated state $m = 1$ mode. Here $H/R = 1.5$, the steady-state axisymmetric streamlines from the base flow are projected over the top of the contours in each case. Light (dark) contours are positive (negative) and the right-hand boundary of each image is the cylinder axis.

the figure, can be associated with (i) the shear layer at the interface between the vortex breakdown bubble and the outer flow, (ii) the wake of the vortex breakdown bubble where swirling flow converges towards the axis, (iii) the location of severe streamline bending after the radially inward flow collides with the vortex breakdown bubble in the meridional plane and (iv) the tip of the wall-jet shear layer. These structures are also shown in figures 11(*a*) and 11(*b*). In figure 10, increasing the level of isocontour from 30 % of maximum to 40 %, we see a significant reduction in the size of structures 2–4 while structure 1 remains strong. Further increase in perturbation strength to 50 % of maximum results in the complete disappearance of structures 2–4 with only structure 1, which is associated with the vortex breakdown bubble, remaining coherent with little dissipation.

Figures 11(*c*) and 11(*d*) show the spatial structures for the $m = 3$ and $m = 1$ modes, respectively, at $Re = 2650$. Here, it can be seen that the major structure associated with the $m = 3$ mode is at its most intense near the tip of the vortex breakdown bubble where fluid, spiralling outward on its return from the free surface, is forced to quickly adjust to the rapid change in curvature of the vortex breakdown bubble and spiral back in towards the axis. This structure can be seen to persist well into the vortex breakdown bubble wake. The $m = 1$ mode at $Re = 2650$ contains the same structures (1 to 4) as the $m = 1$ mode observed at lower Re, except now the relative (azimuthal) positioning of the maxima have changed, such that they can all be observed in a single meridional semi-plane. A similar analysis of the other velocity components (not shown) revealed a similar pattern, albeit involving some different structures, but with structures similar to structure 1 in figure 10 remaining strong; the most significant difference being the existence of the aforementioned large perturbation to the radial velocity at the axis near the rotating base.

The pertinent point is that once again, for this aspect ratio, instability of the free-surface cylinder flow seems to be directly connected to the existence of the vortex breakdown bubble, which has not been found to be the case at other aspect ratios.

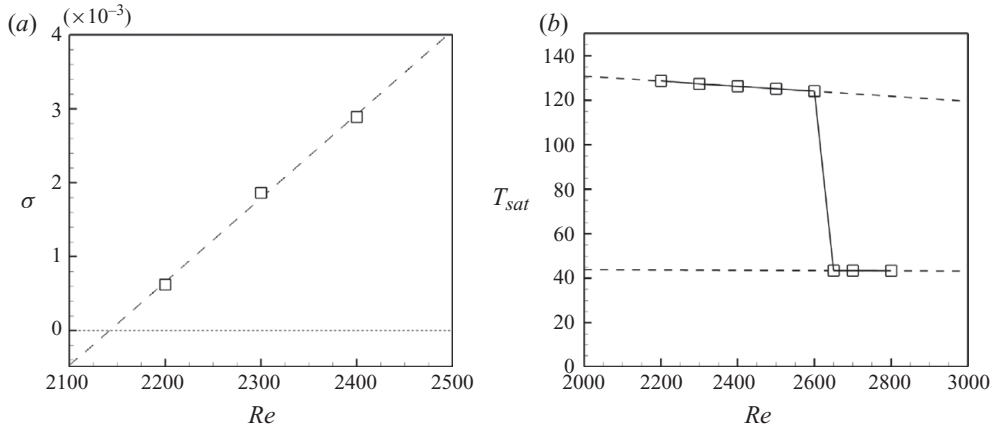

FIGURE 12. (*a*) Estimated growth rates from the 3D DNS plotted against Reynolds number. Dashed line is a linear fit of the data; (*b*) saturated period of the flow against Reynolds number from the 3D DNS.

Finally, figures 12(*a*) and 12(*b*) show measured growth rates and saturated periods, respectively, for the $H/R = 1.5$ cylinder as functions of the Reynolds number. The growth rates were obtained via a nonlinear stability analysis using a Landau model, following the procedure described and used by Sheard, Thompson & Hourigan (2004). Figure 12(*a*) leads to a predicted critical Reynolds number, for the transition from axisymmetric to non-axisymmetric flow, of approximately $Re_c = 2142$. Because of the prohibitive cost of computing saturated 3D solutions at Reynolds numbers close to a transition point (note again the very small growth rates), only three data points were computed. Nevertheless, this predicted critical Reynolds number supports the linear prediction from § 3 of $Re_c = 2152$ to a high degree of accuracy.

Figure 12(*b*) presents a further indication that there is another significant shift in the flow for $Re \gtrsim 2600$, despite the saturated flow field maintaining azimuthal wavenumber $m = 1$ until at least $Re = 2800$ (results not shown). From figure 12(*b*), the saturated 3D flow for $Re \gtrsim 2600$ has a period approximately 1/3 of that of the saturated flow for $Re \lesssim 2600$. It is at about this Reynolds number where the transient $m = 3$ mode was observed, and above this Reynolds number the secondary $m = 1$ mode also becomes dominant (over the primary $m = 1$). Inspection of the angular frequencies associated with the computed linear stability modes revealed that the secondary $m = 1$ mode does indeed have a frequency $f_{1,2} \simeq 2.9 f_{1,1}$. It is the switching between these modes (predicted by linear stability) that causes the change in the saturated period of the (fully 3D) flow for $Re \gtrsim 2600$. Inspection of the time evolution of vorticity isosurfaces and the velocity signal from the monitored points for $Re = 2800$ (not shown) revealed a possible third transition occurring for $Re \gtrsim 2700$, with the flow still maintaining an $m = 1$ spatial structure in the azimuth. With no further $m = 1$ modes predicted by the linear stability analysis, it is unlikely that this third transition is due to further activity in non-axisymmetric modes. Instead, it is likely that the Hopf bifurcation that leads to transition, from a steady to time-periodic state, in the axisymmetric subspace at $Re \backsimeq 2660$ (Lopez 1995; Brøns *et al.* 2001; Iwatsu 2005), manifests in the full 3D flow for $Re \gtrsim 2700$ as a secondary Hopf (Neimark–Sacker) bifurcation due to an instability mode with $m = 0$. Note that the increasing Reynolds number here (relative to the initial transition at $Re = 2152$) renders linear stability theory inaccurate, and due to the prohibitive cost of nonlinear 3D DNS the characteristics and exact location of

this third transition are not further pursued. However, the fact that the bifurcation that manifests in the axisymmetric subspace seems to persist even when the full nonlinearity and three-dimensionality of the dynamics are considered (albeit at a slightly higher value of Re) indicates that the Hopf bifurcation in the axisymmetric subspace is in fact inherent to these flows, and not an artefact of numerical models restricted to axisymmetry.

5. Conclusions

The swirling flow in a circular cylinder of varying aspect ratio with an open top surface, driven by rotation of the base endwall, has been closely investigated using a combination of linear and nonlinear stability analysis and 3D spectral element–Fourier flow simulations. Numerous aspect ratios, hitherto neglected from an axisymmetry-breaking perspective, as well as one previously considered aspect ratio were investigated, with a focus on the $H/R = 1.5$ case. For all aspect ratios, symmetry breaking occurred at Reynolds numbers well below the previously defined stability limits for flows with forced axisymmetry, and also below the symmetry-breaking transitions at corresponding aspect ratios in *enclosed* cylinder flow, as reported by Gelfgat *et al.* (2001) and others. At $H/R = 1.5$, the basic flow state loses stability via a supercritical symmetry-breaking Hopf bifurcation to a rotating wave state characterised by azimuthal wavenumber $m = 1$ at $Re \approx 2150$. The stability analysis predicted a possible secondary bifurcation to an $m = 3$ wave state for approximately $Re \geqslant 2550$, whereas the 3D DNS revealed that this $m = 3$ is a transient state that quickly loses stability to a secondary $m = 1$ mode. The physical mechanisms leading to loss of stability of the basic state were hypothesised to be instability of the weak shear layer at the interface between the slowly recirculating fluid in the vortex breakdown bubble and the relatively faster moving outer fluid. This conclusion is in contrast to previous findings for other cylinder configurations where symmetry breaking occurred as a result of instability in the tip of the wall-jet shear layer, or due to collision of the radially inward flow of fluid in the meridional plane. Both of these phenomena were given consideration in the current study; however, we conclude that the aforementioned instability at the interface of the vortex breakdown bubble boundary is the physical mechanism primarily responsible for symmetry breaking in the open cylinder with $H/R = 1.5$.

For $Re \gtrsim 2600$, a change in the saturated period for the 3D flows in cylinders with $H/R = 1.5$ is associated with the switching of leading $m = 1$ modes of different frequencies. For $Re \gtrsim 2700$, a third transition leading to a state with modulated time signal, but still with $m = 1$ spatial structure, is probably associated with an $m = 0$ mode that causes a change from steady to time-periodic flow states in the axisymmetric subspace, reported to occur at approximately $Re = 2660$ numerous times previously.

There still remains a large portion of the parameter space ($2.0 < H/R < 4.0$) to be investigated, from a 3D nonlinear standpoint, in order to verify the predictions of the linear stability analysis reported here. Our 3D simulations verified the linear stability predictions for the most unstable mode having $m = 1$ and its critical Reynolds number ($Re_c = 2152$) for the $H/R = 1.5$ open cylinder, as well as the existence of a secondary $m = 1$ mode. It also verified, to some extent, the existence of an instability with wavenumber $m = 3$ at higher Reynolds numbers and a further transition related to a mode with $m = 0$. However, they also served as a reminder of the limitations of linear-stability analysis techniques insofar as predicting dominant states (resulting

from secondary or tertiary bifurcations) once the primary bifurcation away from the basic state has occurred.

This research was undertaken in part using the NCI National Facility in Canberra, Australia, thanks to a Merit Allocation Scheme grant. NCI is supported by the Australian Commonwealth Government. The authors thank the Monash University Faculty of Engineering for financial support through its Engineering Small Grants scheme. S.J.C. thanks the Department of Mechanical and Aerospace Engineering at Monash University for ongoing postgraduate scholarship support, and the Monash e-Research Centre for access to their High Performance Computing facility.

REFERENCES

Barkley, D. & Henderson, R. D. 1996 Three-dimensional Floquet stability analysis of the wake of a circular cylinder. *J. Fluid Mech.* **322**, 215–241.

Blackburn, H. M. 2002 Three-dimensional instability and state selection in an oscillatory axisymmetric swirling flow. *Phys. Fluids* **14**, 3983–3996.

Blackburn, H. M. & Lopez, J. M. 2000 Symmetry breaking of the flow in a cylinder driven by a rotating end wall. *Phys. Fluids* **12**, 2698–2701.

Blackburn, H. M. & Lopez, J. M. 2002 Modulated rotating waves in an enclosed swirling flow. *J. Fluid Mech.* **465**, 33–58.

Blackburn, H. M. & Lopez, J. M. 2003 On three-dimensional quasi-periodic Floquet instabilities of two-dimensional bluff body wakes. *Phys. Fluids* **15**, L57–L50.

Blackburn, H. M. & Sherwin, S. J. 2004 Formulation of a Galerkin spectral element-Fourier method for three-dimensional incompressible flows in cylindrical geometries. *J. Comput. Phys.* **197** (2), 759–778.

Bouffanais, R. & Lo Jacono, D. L. 2009 Unsteady transitional swirling flow in the presence of a moving free surface. *Phys. Fluids* **21**, 064107.

Brøns, M., Thompson, M. C. & Hourigan, K. 2009 Dye visualization near a three-dimensional stagnation point: application to the vortex breakdown bubble. *J. Fluid Mech.* **622**, 177–194.

Brøns, M., Voigt, L. K. & Sørensen, J. N. 1999 Streamline topology of steady axisymmetric vortex breakdown in a cylinder with co-and counter-rotating end-covers. *J. Fluid Mech.* **401**, 275–292.

Brøns, M., Voigt, L. K. & Sørensen, J. N. 2001 Topology of vortex breakdown bubbles in a cylinder with a rotating bottom and a free surface. *J. Fluid Mech.* **428**, 133–148.

Brown, G. L. & Lopez, J. M. 1990 Axisymmetric vortex breakdown. Part 2. Physical mechanisms. *J. Fluid Mech.* **221**, 553–576.

Dusting, J., Sheridan, J. & Hourigan, K. 2004 Flows within a cylindrical cell culture bioreactor with a free-surface and a rotating base. In *Proc. of the 15th Australasian Fluid Mechanics Conference* (ed. M. Behnia, W. Lin & G. D. McBain), pp. 501–504. University of Sydney.

Dusting, J., Sheridan, J. & Hourigan, K. 2006 A fluid dynamics approach to bioreactor design for cell and tissue culture. *Biotechnol. Bioengng* **94** (6), 1196–1208.

Escudier, M. P. 1984 Observations of the flow produced in a cylindrical container by a rotating endwall. *Exp. Fluids* **2** (4), 189–196.

Gelfgat, A. Y., Bar-Yoseph, P. Z. & Solan, A. 1996 Confined swirling flow simulation using spectral Galerkin and finite volume methods. *Proc. ASME Fluids Engng Div. Conf.* **238**, 105–111.

Gelfgat, A. Y., Bar-Yoseph, P. Z. & Solan, A. 2001 Three-dimensional instability of axisymmetric flow in a rotating lid-cylinder enclosure. *J. Fluid Mech.* **438**, 363–377.

Gregory, N., Stuart, J. T. & Walker, W. S. 1955 On the stability of three-dimensional boundary layers with application to the flow due to a rotating disk. *Phil. Trans. R. Soc. Lond.* A **248** (943), 155–199.

Gutman, L. N. 1957 Theoretical model of a waterspout. In *Bulletin of the Academy of Science USSR,* pp. 87–103.

Hirsa, A. H., Lopez, J. M. & Miraghaie, R. 2002 Symmetry breaking to a rotating wave in a lid-driven cylinder with a free surface: experimental observation. *Phys. Fluids* **14**, L29–L32.

Husain, H. S., Shtern, V. & Hussain, F. 2003 Control of vortex breakdown by addition of near-axis swirl. *Phys. Fluids* **15**, 271–279.

Iwatsu, R. 2005 Numerical study of flows in a cylindrical container with rotating bottom and top flat free surface. *J. Phys. Soc. Japan* **74** (1), 333–344.

Karniadakis, G. E., Israeli, M. & Orszag, S. A. 1991 High-order splitting methods for the incompressible Navier–Stokes equations. *J. Comput. Phys.* **97** (2), 414–443.

Lo Jacono, D., Sørensen, J. N., Thompson, M. C. & Hourigan, K. 2008 Control of vortex breakdown in a closed cylinder with a small rotating rod. *J. Fluids Struct.* **24** (8), 1278–1283.

Lo Jacono, D. L., Nazarinia, M. & Brøns, M. 2009 Experimental vortex breakdown topology in a cylinder with a free surface. *Phys. Fluids* **21**, 111704.

Lopez, J. M. 1990 Axisymmetric vortex breakdown. Part 1. Confined swirling flow. *J. Fluid Mech.* **221**, 533–552.

Lopez, J. M. 1995 Unsteady swirling flow in an enclosed cylinder with reflectional symmetry. *Phys. Fluids* **7**, 2700–2714.

Lopez, J. M. 2006 Rotating and modulated rotating waves in transitions of an enclosed swirling flow. *J. Fluid Mech.* **553**, 323–346.

Lopez, J. M., Cui, Y. D. & Lim, T. T. 2006 Experimental and numerical investigation of the competition between axisymmetric time-periodic modes in an enclosed swirling flow. *Phys. Fluids* **18**, 104106.

Lopez, J. M., Hart, J. E., Marques, F., Kittelman, S. & Shen, J. 2002 Instability and mode interactions in a differentially driven rotating cylinder. *J. Fluid Mech.* **462**, 383–409.

Lopez, J. M. & Marques, F. 2004 Mode competition between rotating waves in a swirling flow with reflection symmetry. *J. Fluid Mech.* **507**, 265–288.

Lopez, J. M., Marques, F., Hirsa, A. H. & Miraghaie, R. 2004 Symmetry breaking in free-surface cylinder flows. *J. Fluid Mech.* **502**, 99–126.

Lopez, J. M., Marques, F. & Sanchez, J. 2001 Oscillatory modes in an enclosed swirling flow. *J. Fluid Mech.* **439**, 109–129.

Lopez, J. M. & Perry, A. D. 1992 Axisymmetric vortex breakdown. Part 3. Onset of periodic flow and chaotic advection. *J. Fluid Mech.* **234**, 449–471.

Marques, F. & Lopez, J. M. 2001 Precessing vortex breakdown mode in an enclosed cylinder flow. *Phys. Fluids* **13**, 1679–1682.

Marques, F., Lopez, J. M. & Shen, J. 2002 Mode interactions in an enclosed swirling flow: a double Hopf bifurcation between azimuthal wavenumbers 0 and 2. *J. Fluid Mech.* **455**, 263–281.

Mununga, L., Hourigan, K., Thompson, M. C. & Leweke, T. 2004 Confined flow vortex breakdown control using a small rotating disk. *Phys. Fluids* **16**, 4750–4753.

Serre, E. & Bontoux, P. 2007 Vortex breakdown in a cylinder with a rotating bottom and a flat stress-free surface. *Intl J. Heat Fluid Flow* **28** (2), 229–248.

Sheard, G. J. 2009 Flow dynamics and wall shear-stress variation in a fusiform aneurysm. *J. Engng Maths* **64** (4), 379–390.

Sheard, G. J., Fitzgerald, M. J. & Ryan, K. 2009 Cylinders with square cross-section: wake instabilities with incidence angle variation. *J. Fluid Mech.* **630**, 43–69.

Sheard, G. J. & Ryan, K. 2007 Pressure-driven flow past spheres moving in a circular tube. *J. Fluid Mech.* **592**, 233–262.

Sheard, G. J., Thompson, M. C. & Hourigan, K. 2004 From spheres to circular cylinders: non-axisymmetric transitions in the flow past rings. *J. Fluid Mech.* **506**, 45–78.

Sørensen, J. N., Naumov, I. & Mikkelsen, R. 2006 Experimental investigation of three-dimensional flow instabilities in a rotating lid-driven cavity. *Exp. Fluids* **41** (3), 425–440.

Sotiropoulos, F. & Ventikos, Y. 2001 The three-dimensional structure of confined swirling flows with vortex breakdown. *J. Fluid Mech.* **426**, 155–175.

Spohn, A., Mory, M. & Hopfinger, E. J. 1993 Observations of vortex breakdown in an open cylindrical container with a rotating bottom. *Exp. Fluids* **14** (1), 70–77.

Spohn, A., Mory, M. & Hopfinger, E. J. 1998 Experiments on vortex breakdown in a confined flow generated by a rotating disc. *J. Fluid Mech.* **370**, 73–99.

Stevens, J. L., Lopez, J. M. & Cantwell, B. J. 1999 Oscillatory flow states in an enclosed cylinder with a rotating endwall. *J. Fluid Mech.* **389**, 101–118.

Tan, B. T., Liow, K. Y. S., Mununga, L., Thompson, M. C. & Hourigan, K. 2009 Simulation of the control of vortex breakdown in a closed cylinder using a small rotating disk. *Phys. Fluids* **21**, 024104 (1–8).

Tatro, P. R. & Mollo-Christensen, E. L. 1967 Experiments on Ekman layer instability. *J. Fluid Mech.* **28** (3), 531–543.

Thompson, M. C. & Hourigan, K. 2003 The sensitivity of steady vortex breakdown bubbles in confined cylinder flows to rotating lid misalignment. *J. Fluid Mech.* **496**, 129–138.

Vyazmina, E., Nichols, J. W., Chomaz, J. M. & Schmid, P. J. 2009 The bifurcation structure of viscous steady axisymmetric vortex breakdown with open lateral boundaries. *Phys. Fluids* **21**, 074107.